nature chemistry

ARTICLES

PUBLISHED ONLINE: 28 APRIL 2014 | DOI: 10.1038/NCHEM.1934

Genetically encoded reporters for hyperpolarized xenon magnetic resonance imaging

Mikhail G. Shapiro[1,2,3,4]*, R. Matthew Ramirez[5,6], Lindsay J. Sperling[6], George Sun[2], Jinny Sun[5], Alexander Pines[5,6], David V. Schaffer[2,7] and Vikram S. Bajaj[5,6]*

Magnetic resonance imaging (MRI) enables high-resolution non-invasive observation of the anatomy and function of intact organisms. However, previous MRI reporters of key biological processes tied to gene expression have been limited by the inherently low molecular sensitivity of conventional ^{1}H MRI. This limitation could be overcome through the use of hyperpolarized nuclei, such as in the noble gas xenon, but previous reporters acting on such nuclei have been synthetic. Here, we introduce the first genetically encoded reporters for hyperpolarized ^{129}Xe MRI. These expressible reporters are based on gas vesicles (GVs), gas-binding protein nanostructures expressed by certain buoyant microorganisms. We show that GVs are capable of chemical exchange saturation transfer interactions with xenon, which enables chemically amplified GV detection at picomolar concentrations (a 100- to 10,000-fold improvement over comparable constructs for ^{1}H MRI). We demonstrate the use of GVs as heterologously expressed indicators of gene expression and chemically targeted exogenous labels in MRI experiments performed on living cells.

Genetically encoded optical reporters, such as the green fluorescent protein (GFP), have enabled important advances in biology by making it possible to image cellular and molecular processes, such as gene expression[1]. However, as light is scattered strongly by tissues, fluorescent and bioluminescent reporters are inadequate for many studies of living organisms. By contrast, magnetic resonance imaging (MRI) routinely delivers non-invasive images of anatomy at high resolution[2]. Thus, there has been a long-standing interest in developing analogues of GFP for MRI[3]. Unfortunately, previous efforts to develop such reporters have yielded constructs with low molecular sensitivity. This limitation arises because all such reporters produce signal changes via their effect on thermally polarized ^{1}H nuclei, and must therefore be present in biological specimens at concentrations sufficient to interact with a substantial fraction of the nuclei, ~100 molar ^{1}H (primarily in H_2O), on subsecond timescales[4]. As a result, practical detection limits were in the micromolar range[3,4] compared to the nanomolar range for GFP[5].

This sensitivity barrier can be overcome through the use of hyperpolarized MRI. This form of imaging exploits nuclei that can be hyperpolarized (prepared in non-equilibrium states of artificially high spin polarization) and introduced into the body by injection or inhalation[6,7]. In particular, the spin polarization of ^{129}Xe can be increased 10,000-fold by spin-exchange optical pumping[8], such that its magnetic resonance signal in a saturated aqueous solution at millimolar concentrations is comparable to that of ~110 molar thermally polarized ^{1}H. After introduction by inhalation, this mostly inert and biocompatible element distributes rapidly into tissues such as the lungs[9], brain[10], heart and kidneys[11], where its non-equilibrium polarization is maintained over a lifetime (T_1) of 4–16 seconds[12,13]. As the signals measured in these tissues arise from ^{129}Xe concentrations several orders of magnitude lower than that of water, the detectable concentrations of xenon-active MRI reporters (that is, the concentrations needed to interact with a substantial fraction of the xenon and alter its signal) should themselves be much lower than their ^{1}H counterparts.

Previous work on molecular reporters for hyperpolarized ^{129}Xe MRI focused on synthetic xenon-binding constructs, such as cryptophanes[14–16] or perfluorocarbon droplets[17], that alter the magnetic resonance frequency of bound ^{129}Xe. These reporters can be detected directly via their bound-xenon chemical peak or through chemical exchange saturation transfer (HyperCEST)[18,19]. In the latter approach, saturation pulses are applied at the chemical shift of xenon bound to the reporter and a rapid exchange between reporter-bound and dissolved xenon results in saturation transfer between these two compartments, which reduces the signal in the dissolved xenon pool. Using this amplified detection scheme, synthetic HyperCEST reporters are detectable at nanomolar or lower concentrations[17,20–22]. However, despite recent progress[23–27], synthetic constructs remain challenging to produce and difficult to deliver to cells or link to specific biological processes. It is therefore highly desirable to develop HyperCEST reporters encoded by genes, although this would at first appear difficult because xenon, a noble gas, interacts with proteins only weakly.

To overcome this challenge, we turned to a unique class of genetically encoded gas nanostructures from buoyant microbes. Gas vesicles (GVs) are nanoscale gas compartments (typically 50–500 nm in size) formed entirely from protein that are expressed in several species of waterborne halobacteria and cyanobacteria as a means to control buoyancy and thereby migrate to optimal depths for access to light and nutrients[28,29]. The contents of the GVs are in constant exchange with gas molecules dissolved in the surrounding media, and they are permeable to gases that range in size from hydrogen to perfluorocyclobutane[30]. GVs mostly comprise copies of

[1]Miller Research Institute, University of California, Berkeley, Berkeley, California 94720, USA, [2]Department of Bioengineering, University of California, Berkeley, Berkeley, California 94720, USA, [3]Department of Molecular and Cell Biology, University of California, Berkeley, Berkeley, California 94720, USA, [4]Division of Chemistry and Chemical Engineering, California Institute of Technology, Pasadena, California 91125, USA, [5]Department of Chemical and Biomolecular Engineering, University of California, Berkeley, Berkeley, California 94720, USA, [6]Materials Science Division, Lawrence Berkeley National Laboratory, Berkeley, California 94720, USA, [7]Department of Chemistry, University of California, Berkeley, Berkeley, California 94720, USA.
*e-mail: mikhail@caltech.edu; vikbajaj@gmail.com

© 2014 Macmillan Publishers Limited. All rights reserved.

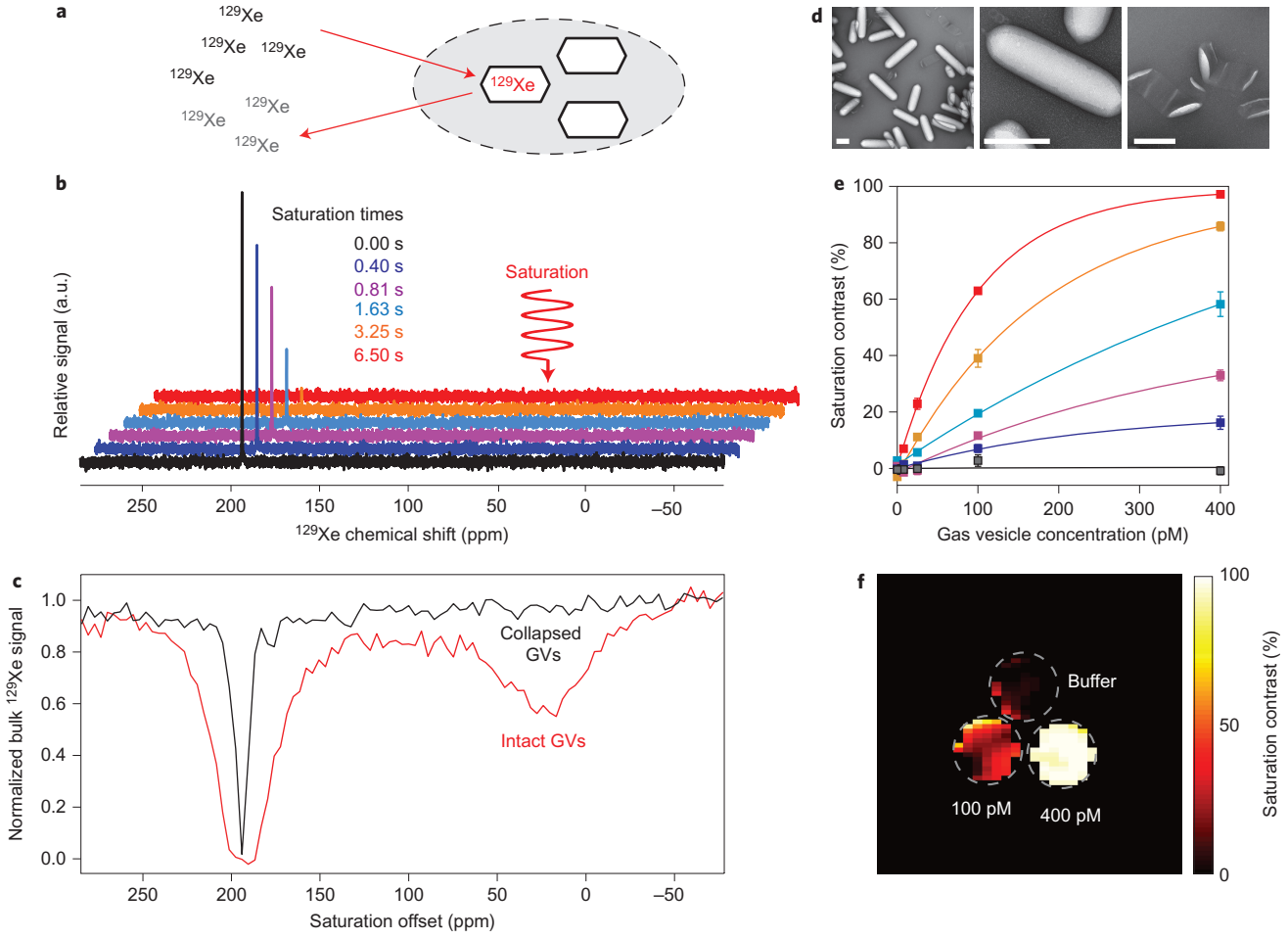

Figure 1 | GVs produce HyperCEST contrast at picomolar concentrations. a, Diagram of ^{129}Xe chemical exchange saturation transfer between bulk aqueous solvent (left) and GVs (hexagons) either in isolation or inside a cell (grey). Polarized ^{129}Xe nuclei (black) exchange into GVs, where they have a unique NMR frequency (red) at which they can be saturated by RF pulses. Saturated (grey) xenon returns to the bulk, which causes a decrease in bulk ^{129}Xe signal. **b**, NMR spectra of ^{129}Xe in buffer that contained 400 pM GVs after saturation for the specified amount of time at 31.2 ppm. Spectra are offset for visibility. a.u., arbitrary units. **c**, Frequency-dependent saturation spectra for intact (red) and collapsed (black) GVs. Each spectrum is an average of two. **d**, Transmission electron micrographs of intact (left and centre) and collapsed (right) GVs used in this study. Scale bars, 200 nm. **e**, Concentration dependence of saturation contrast generated by GVs with saturation times that correspond colour-wise to those in **b** ($n = 3$ for each data point). Data are fitted with monoexponential curves as a visual aide. **f**, Saturation contrast image of a three-compartment phantom that contains 400 pM GVs, 100 pM GVs and buffer. RF saturation and image-averaging parameters are listed in Supplementary Tables 1 and 2. All the GVs used here were isolated from *A. flos-aquae*. Error bars represent s.e.m.

a single highly conserved protein, GvpA, but their formation requires at least eight genes contained in GV gene clusters[28]. A six kilobase cluster that encodes 11 GV genes has been expressed heterologously in *E. coli*, which resulted in the formation of GVs and increased cellular buoyancy[31]. We hypothesized that dissolved ^{129}Xe would partition into GVs, where it would form a gaseous phase with a distinct chemical shift, and would rapidly exchange between GVs and solution, thus enabling the use of these nanostructures as genetically encoded HyperCEST reporters (Fig. 1a). We also hypothesized that GVs from different species, which have distinct shapes and sizes, would have different chemical shifts and so allow multiplexed imaging.

Results

GVs produce HyperCEST contrast at picomolar concentrations. We tested the ability of GVs isolated from *Anabaena flos-aquae* to produce HyperCEST contrast in aqueous solutions that contained hyperpolarized ^{129}Xe at 9.4 T. The GVs were released from cells by hypertonic lysis and purified by centrifugally assisted flotation, and their concentration, purity, monodispersity and integrity were determined by total-protein assay and transmission electron microscopy (TEM) (see Methods). These nanostructures have a diameter of approximately 145 nm and lengths that range from 250 to 1,000 nm (Fig. 1d, Supplementary Fig. 1a).

At GV nanostructure concentrations of up to 400 pM, no NMR signal other than the main dissolved xenon peak was detectable (Fig. 1b, black). However, radiofrequency (RF) saturation applied at an offset of 31.2 ppm (relative to gaseous xenon) produced a dramatic decrease in the dissolved ^{129}Xe signal in a saturation-time and power-dependent manner (Fig. 1b). After 6.5 seconds of exposure to a 33.6 μT (396 Hz) continuous-wave field, the dissolved xenon signal was completely saturated. We measured this signal as a function of saturation frequency, which revealed a unique GV saturation peak at 31.2 ppm, in addition to the saturation peak for free xenon at 195 ppm (Fig. 1c, red). As a control, we irreversibly collapsed GVs through the application of hydrostatic pressure before performing NMR spectroscopy (Fig. 1d). These collapsed GVs no longer produced saturation contrast, which confirms that their gas-filled interior was responsible for this effect (Fig. 1c, black). The presence of intact GVs broadened the direct saturation peak of aqueous ^{129}Xe and the xenon signal itself (Supplementary Fig. 2). Such broadening is characteristic of a chemical exchange

© 2014 Macmillan Publishers Limited. All rights reserved.

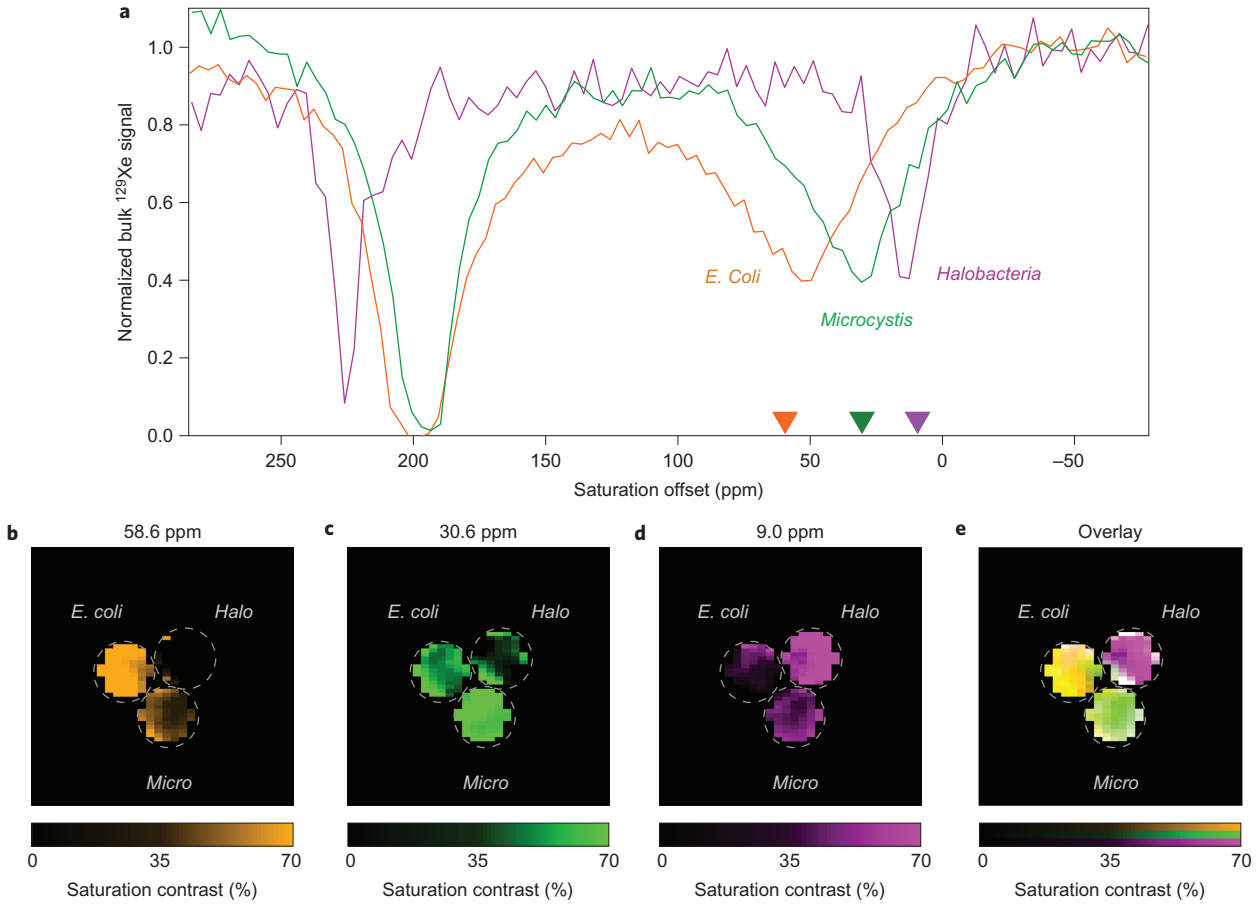

Figure 2 | GVs in different species of bacteria have distinct HyperCEST saturation frequencies, which enables multiplexed imaging. **a**, Frequency-dependent saturation spectra for solutions of wild-type *Halobacteria* sp. NRC-1 ($D_{600} = 0.01$), *Microcystis* sp. ($D_{600} = 0.36$) and *E. coli* heterologously expressing the pNL29 GV gene cassette from *B. megaterium* ($D_{600} = 4.46$) ($n = 3$ for each data point). Colour triangles on the *x* axis indicate the frequency offsets of saturation applied to generate the images in **b**–**d**. **b**–**d**, Pseudocoloured saturation contrast images of a three-compartment phantom that contains *Microcystis* sp. ($D_{600} = 1.2$), *E. coli* expressing pNL29 ($D_{600} = 5.8$) and purified GVs from *Halobacteria* sp. NRC-1 ($D_{500,PS} = 0.32$). Saturation was applied at offsets of 58.6 ppm (**b**), 30.6 ppm (**c**) and 9.0 ppm (**d**). **e**, Colour overlay of **b**–**d**. RF saturation and image-averaging parameters are listed in Supplementary Tables 1 and 2.

mechanism, as previously observed with ^{1}H CEST agents[32–34]. It may additionally result from the magnetic susceptibility difference between gas-containing GVs and the media.

To determine the molecular sensitivity of GVs as an MRI reporter, we performed HyperCEST measurements across a range of GV concentrations and saturation times (Fig. 1e). With 6.5 seconds of saturation at 31.2 ppm, 8 pM GVs were sufficient to produce a $7.0 \pm 0.4\%$ saturation contrast (defined as the difference in aqueous ^{129}Xe signal after on-resonance saturation relative to an off-resonance control); with 400 pM GVs, saturation contrast reached $97.2 \pm 1.0\%$. With saturation times of 0.4 and 0.8 seconds, which are much shorter than the *in vivo* T_1 of ^{129}Xe, 400 pM GVs produced saturation contrasts of $16.2 \pm 2.3\%$ and $33.0 \pm 1.9\%$, respectively, and a statistically significant contrast was observed at 25 pM with a realistic saturation time of 1.63 seconds. Thus, GV HyperCEST reporters have a molecular sensitivity in the mid-picomolar range. We used HyperCEST MRI to image GVs in a three-compartment phantom that contained buffer, 100 pM GVs or 400 pM GVs. Nearly complete saturation could be seen in the 400 pM chamber; significant saturation contrast was also present at the lower concentration (Fig 1f).

Unique chemical shifts of GVs from different species enable multiplexed imaging. To test our hypothesis that differences in the shape and size of GVs encoded in diverse bacterial species would result in distinct HyperCEST saturation frequencies, we acquired saturation spectra as a function of frequency from solutions that contained intact *Halobacteria* sp. NRC-1, *Microcystis* sp. and *E. coli* cells in their appropriate media. The first two species expressed native GV genes; the *E. coli* were transformed with a plasmid that contained a minimal GV-forming gene cluster from *Bacillus megaterium*[31]. As hypothesized, each species had a unique saturation-frequency profile, with maximal saturation at 14.4 ppm, 30.6 ppm and 51.4 ppm for *Halobacteria* sp. NRC-1, *Microcystis* sp. and *E. coli*, respectively (Fig. 2a). These distinct saturation profiles enabled multiplexed MRI to be performed by applying saturation at three different frequencies (Fig. 2b–e), the result being analogous to fluorescent imaging using GFP derivatives with distinct optical spectra. The downfield-shifted aqueous xenon peak in the halobacterial spectrum at 226 ppm probably resulted from the high salt content of its media (25% NaCl); this shift was also evident in the corresponding media-only saturation spectrum (Supplementary Fig. 3). In addition, GVs purified from *Halobacteria* sp. NRC-1 into a low-salt buffer (shown in the TEM image in Supplementary Fig. 1b) produced a broadened aqueous xenon saturation peak centred at the more typical 195 ppm, with the peak attributable to GVs still centred at approximately 14.4 ppm (Supplementary Fig. 4). Finally, purified *Halobacteria* sp. NRC-1 GVs were used in place of intact cells in the magnetic resonance images shown in Fig. 2b–e so that the dissolved xenon

© 2014 Macmillan Publishers Limited. All rights reserved.

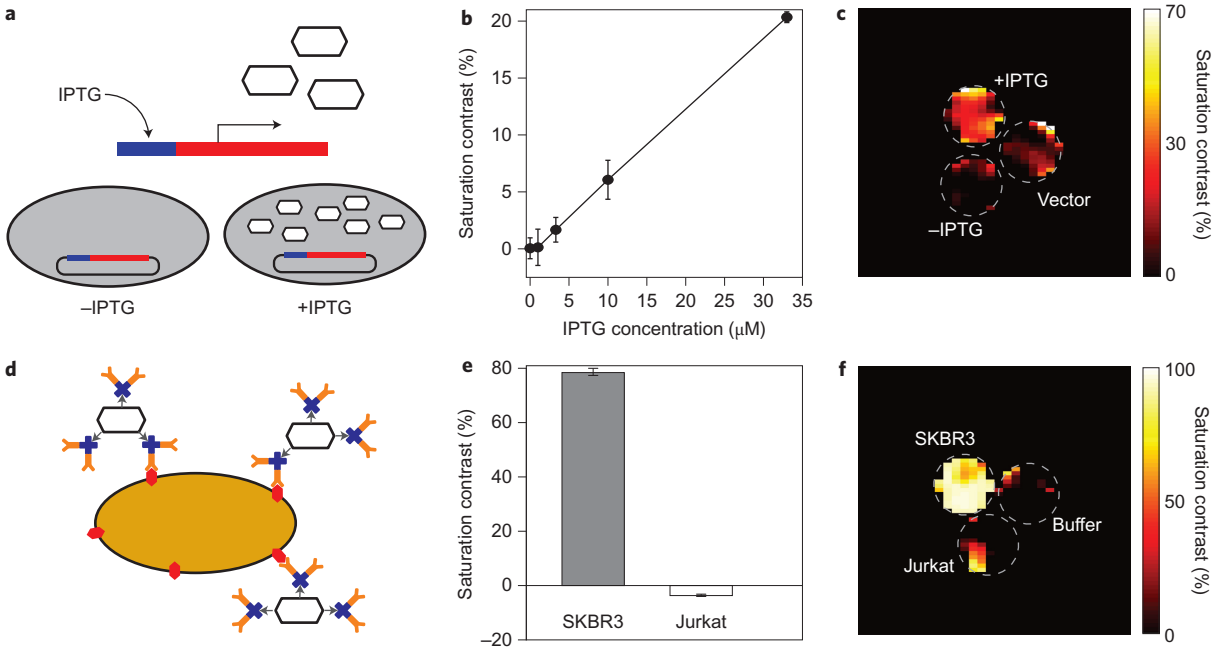

Figure 3 | GVs as genetic reporters and biosensors. a, Diagram of inducible GV expression in *E. coli*. cells (grey ovals) contain the pNL29 gene cluster (red) under the control of an IPTG-inducible promoter (blue). GVs (black) are only produced when IPTG is present. **b**, Saturation contrast generated by *E. coli* ($D_{600} = 0.32$) that contained IPTG-inducible pNL29 after overnight supplementation with different quantities of IPTG ($n = 4$ for each data point). A straight line is fitted to the data as a visual aide. **c**, Saturation contrast image of a three-compartment phantom that contained *E. coli* ($D_{600} = 1.6$) carrying IPTG-inducible pNL29, with and without overnight induction with 50 μM IPTG, or an empty control vector induced with 50 μM IPTG. **d**, Diagram of cancer-cell labelling strategy. *Anabaena flos-aquae* GVs (black) are functionalized with anti-HER2 antibodies (orange) via biotin–avidin conjugation (grey, blue). The antibody recognizes the HER2 receptor (red) on SKBR3 cells. **e**, Saturation contrast generated by GV-labelled SKBR3 or Jurkat cells ($n = 3$ for each data point). **f**, Saturation contrast image of three-compartment phantom that contained SKBR3 cells labelled with antibody-functionalized GVs, similarly labelled Jurkat cells and unlabelled SKBR3 cells. RF saturation and image-averaging parameters are listed in Supplementary Tables 1 and 2. Error bars represent s.e.m.

resonance peak would be consistent across specimens for the purpose of pulse programming.

Heterologously expressed GVs enable quantitative imaging of gene expression. We tested the ability of GVs to act as quantitative reporters of gene expression by placing their expression in *E. coli* under the control of a promoter inducible by isopropyl β-D-1-thiogalactopyranoside (IPTG, Fig. 3a). Overnight induction with IPTG resulted in GV expression (TEM image in Supplementary Fig. 1c) and a robust HyperCEST image contrast that was absent from cells that were not induced and from induced cells that contained a control vector lacking GV genes (Fig. 3b,c). The magnitude of HyperCEST contrast was dependent on the dose of IPTG, which confirms the utility of GVs as quantitative reporters of gene expression.

Chemically functionalized GVs enable non-invasive labelling of breast cancer cells. To assess the potential utility of GVs as targeted biosensors, we functionalized purified GVs from *A. flos-aquae* with biotin via *N*-hydroxysuccinimide linkages to lysine side chains on the GV surface and attached streptavidin-functionalized antibodies against the HER2 receptor (Fig. 3d). Anti-HER2 GVs were used to label the HER2-expressing breast cancer cell line SKBR3 or control Jurkat cells. HyperCEST imaging easily distinguished a suspension of labelled SKBR3 cells from identically treated Jurkat cells (Fig. 3e,f). The targeted breast cancer cells exhibited a saturation contrast of $78.53 \pm 1.38\%$.

Pharmacokinetic modelling suggests the feasibility of *in vivo* ^{129}Xe HyperCEST. The use of GVs in animals as genetically encoded or injected reporters will require the development of methods for *in vivo* HyperCEST imaging. Although ^{129}Xe MRI of tissues is still in its relative infancy, hyperpolarized xenon dissolved after inhalation has been imaged robustly in highly vascularized organs such as the brain[10,13,35,36]. To assess the feasibility of combining this imaging approach with GV HyperCEST, we adapted published pharmacokinetic models of inhaled hyperpolarized ^{129}Xe (refs 37,38) to include a saturation and imaging pulse sequence (using methods and parameters detailed in the Supplementary Information and Supplementary Tables 3 and 4). Consistent with previous findings, our model predicted a peak brain-tissue concentration of 22 μM hyperpolarized ^{129}Xe, assuming the inhalation of isotopically enriched ^{129}Xe polarized to 10% (Supplementary Figs 5 and 6). This would result in an MRI signal-to-noise ratio 64-fold lower than that of protons[38], but substantially higher than the that of ^{19}F MRI, which is increasingly used for molecular imaging[39]. Importantly, although ^{129}Xe magnetization is non-renewable, our model confirms that the combination of repeated xenon inhalation and low flip-angle sequences permits continuous imaging[10,35,36] (Supplementary Fig. 6a,b). On the application of an on-resonance saturation pulse, the model predicts a 73% signal decrease in GV-containing regions (compared to an off-resonance control) and minimal change in regions devoid of GVs (Supplementary Fig. 6b,c). That this detection scheme is ratiometric (that is, internally normalized by measuring the signal in a given voxel with and without an on-resonance saturation pre-pulse) should make GV imaging relatively robust to any spatial inhomogeneity in the distribution of xenon in the target tissue. Overall, these modelling results support the feasibility of imaging GV-based HyperCEST reporters in the brain and similarly vascularized organs, which can be explored in future experimental studies.

© 2014 Macmillan Publishers Limited. All rights reserved.

Discussion

Our results establish GVs as the first genetically encoded molecular reporters for hyperpolarized MRI. Compared to analogous ^{1}H-CEST reporter genes[40], the detection limit of GVs represents an *in vitro* sensitivity improvement of 10,000-fold and 100-fold in terms of molar concentration (25 pM) and protein mass ($\sim$2.5 μg ml^{-1}), respectively. Furthermore, because genetic variation in the shape, size and/or chemical properties of GVs from different species results in unique ^{129}Xe offset frequencies, it is possible to perform multiplexed imaging of GVs analogous to multicolour fluorescent protein microscopy[1]. Although such multiplexing has also been shown with ^{1}H MRI CEST constructs[41] and magnetic microstructures[42], typically the former were used at millimolar concentrations, and the latter are not encoded genetically.

The ability of GVs to label and quantify gene expression in bacteria, as demonstrated here, may have utility in various synthetic biological applications[43] and studies of host–microbe symbiosis[44], immune defence[45] and tumour growth[46]. GV expression in mammalian cells would additionally permit non-invasive imaging of stem-cell migration, immune function, tumour metastasis and other biological processes that involve cell expansion, migration and gene expression. At approximately six kilobases, the size of minimal GV gene clusters is compatible with the capacity of lentiviral vectors for cell transduction and labelling[47]. In addition, standard chemical conjugation makes it possible to use GVs as exogenous molecular labels, as shown here with the detection of breast cancer cells. Further engineering of the biochemical properties of GVs may also be possible at the genetic level, for example by creating fusion constructs of GV proteins with functionalities for targeting or for altered biodistribution[48]. Additionally, given the relative ease of growing large quantities of bacteria and the straightforward purification of GVs based on buoyancy, these imaging agents lend themselves to widespread production and use.

For *in vivo* imaging, GVs expressed in cells, encoded in viral vectors or formulated in a purified, biofunctionalized form could be injected into target tissues or systemic circulation. The resulting distribution of GVs in the body would be revealed subsequently by ^{129}Xe MRI using the HyperCEST technique. Although such *in vivo* imaging was not attempted experimentally, our pharmacokinetic model suggests that it is feasible using inhaled hyperpolarized xenon. In addition, alternative methods of xenon delivery, such as through lipid emulsions[49] and extracorporeal membrane gas exchange[50], may further improve the strength and consistency of tissue ^{129}Xe MRI signals. Importantly, with HyperCEST imaging the timing, route and kinetics of xenon delivery are independent of the expression or delivery of GVs and may be optimized separately. Continuing advances in *in vivo* ^{129}Xe MRI combined with, and stimulated by, the introduction of the first genetically encoded reporters for this modality promise to deliver the sensitivity advantages of hyperpolarization to a broader range of biological imaging applications.

Methods

A detailed description of the materials and methods is provided in the Supplementary Information.

Specimen preparation. *Microcystis* sp. (CCAP strain 1450/13), *A. flos-aquae* (CCAP strain 1403/13F) and *Halobacteria* sp. NRC-1 were cultured using standard methods. GVs were isolated using tonic lysis and purified by repeated centrifugally assisted flotation into Tris–HCl buffer. Collapse was performed through the manual application of hydrostatic pressure to GVs inside a capped syringe prior to spectroscopy or imaging. GV concentrations were estimated by pressure-sensitive attenuance at 500 nm ($D_{500,PS}$) calibrated by the results of a bicinchoninic acid assay. The lysis of *A. flos-aquae* cells yielded 0.66$\pm$0.10 nmol GV per gram of dry cell pellet ($n = 4$). Intact microorganisms were imaged in their applicable growth media. The pNL29 GV gene cluster from *B. megaterium* was expressed in BL21 DE3 *E. coli* in an IPTG-inducible plasmid. Cells were induced at $D_{600} \approx 0.4$ and grown overnight at 30 °C. If necessary, cells were concentrated using a 0.22 μm filter. Imaging of *E. coli* was performed in phosphate buffered saline (PBS). For mammalian experiments, SKBR3 and Jurkat cells were cultured in standard media. Prior to imaging, they were harvested and washed with PBS that contained 2% bovine serum albumin (BSA). Anti-HER2 GVs were prepared by chemically biotinylating *A. flos-aquae* GVs using sulfo-NHS-LC-biotin (6-(biotinamidohexanoylamido)hexanoic acid 3-sulfo-N-hydroxysuccinimide ester sodium salt) and purified by centrifugally assisted flotation, and then streptavidin-conjugated anti-HER2 antibodies (clone N12) were attached. Cells were incubated with 400 pM functionalized GVs in PBS with 2% BSA for one hour at 4 °C, washed twice and resuspended in 0.6 ml PBS.

Hyperpolarized ^{129}Xe spectroscopy and imaging. ^{129}Xe NMR and MRI were performed using a 9.4 T spectrometer with dual-tuned 5 mm and 10 mm probes. Hyperpolarized xenon was prepared in continuous mode from a gas mixture of 2% Xe (natural abundance), 10% N_2 and 88% He by spin-exchange optical pumping, using a home-built polarizing apparatus, to a polarization of approximately 2%. Hyperpolarized gas was bubbled into custom phantoms through capillary tubes under 1.57–1.7 atm. A ten second bubble period was followed by a five second wait period to allow bubbles to dissipate and the solution to settle. Chemical shifts were referenced to gaseous ^{129}Xe. Saturation was applied using continuous wave pulses (the parameters are specified in Supplementary Table 1). Saturation contrast represents the normalized difference between on-resonance and off-resonance signals. Frequency-dependent saturation spectra were obtained by measuring the aqueous ^{129}Xe signal as a function of saturation pulse offset, varied from −77.2 ppm to 284.4 ppm. Imaging was performed in a three-compartment phantom inside a 10 mm probe. Xenon images were generated with a fast spin echo (FSE) sequence with eight-echo trains and 10 ms echo time. Including bubbling, wait and saturation times, the overall repetition time (TR) was 17.58 or 19.08 seconds. Other image parameters are listed in Supplementary Table 2. All images were axial without slice selection, and the *k*-space matrix comprised 32 points in the readout dimension and 16 phase-encoding points. The field of view was 20 mm by 20 mm. Image processing included zero-filling the *k*-space matrix 2× in each dimension and thresholding images at 3× root mean square noise. Saturation maps were produced by comparing off-resonance and on-resonance ^{129}Xe images (Supplementary Fig. 7). Proton images were also acquired with a FSE imaging sequence (TR = 1.5 s, echo time = 16.7 ms, four echoes per excitation) without slice selection, with 192 points in both readout and phase-encode dimensions over the 20 mm by 20 mm field of view. Signals were acquired with a 20.16 kHz spectral width and 9.52 ms acquisition time. After data collection, raw free-induction decay signals were processed in MATLAB (The MathWorks). Data and error bars in the figures represent means and standard errors of the mean of *n* biological replicates, as stated in the figure legends.

TEM. TEM images were obtained on a Philips/FEI (Hillsboro) Tecnai 12 microscope operating at 120 kV. GV samples were negatively stained with 2% uranyl acetate and deposited on a carbon-coated formvar grid. Thin-section TEM *E. coli* specimens were prepared by fixing the cells in glutaraldehyde, osmium tetroxide and ferrous cyanide, dehydrating in acetone, embedding in epoxy resin and sectioning under ambient pressure.

Pharmacokinetic model. Pharmacokinetic modelling was performed in MATLAB using the equations, assumptions and parameters described in Supplementary Section 4 and Supplementary Tables 3 and 4.

Received 28 May 2013; accepted 24 March 2014; published online 28 April 2014

References

1. Lippincott-Schwartz, J. & Patterson, G. H. Development and use of fluorescent protein markers in living cells. *Science* **300,** 87–91 (2003).
2. Lauterbur, P. C. Image formation by induced local interactions: examples employing nuclear magnetic resonance. *Nature* **242,** 190–191 (1973).
3. Gilad, A. A., Winnard, P. T. Jr, van Zijl, P. C. & Bulte, J. W. Developing MR reporter genes: promises and pitfalls. *NMR Biomed.* **20,** 275–290 (2007).
4. Shapiro, M. G., Atanasijevic, T., Faas, H., Westmeyer, G. G. & Jasanoff, A. Dynamic imaging with MRI contrast agents: quantitative considerations. *Magn. Reson. Imaging* **24,** 449–462 (2006).
5. Patterson, G. H., Knobel, S. M., Sharif, W. D., Kain, S. R. & Piston, D. W. Use of the green fluorescent protein and its mutants in quantitative fluorescence microscopy. *Biophys. J.* **73,** 2782–2790 (1997).
6. Albert, M. S. *et al.* Biological magnetic resonance imaging using laser-polarized ^{129}Xe. *Nature* **370,** 199–201 (1994).
7. Ardenkjaer-Larsen, J. H. *et al.* Increase in signal-to-noise ratio of >10,000 times in liquid-state NMR. *Proc. Natl Acad. Sci. USA* **100,** 10158–10163 (2003).
8. Walker, T. G. & Happer, W. Spin-exchange optical pumping of noble-gas nuclei. *Rev. Mod. Phys.* **69,** 629–642 (1997).
9. Driehuys, B. *et al.* Imaging alveolar–capillary gas transfer using hyperpolarized ^{129}Xe MRI. *Proc. Natl Acad. Sci. USA* **103,** 18278–18283 (2006).
10. Swanson, S. D. *et al.* Brain MRI with laser-polarized ^{129}Xe. *Magn Reson Med* **38,** 695–698 (1997).

© 2014 Macmillan Publishers Limited. All rights reserved.

11. Swanson, S. D., Rosen, M. S., Coulter, K. P., Welsh, R. C. & Chupp, T. E. Distribution and dynamics of laser-polarized ^{129}Xe magnetization *in vivo*. *Magn. Reson. Med.* **42,** 1137–1145 (1999).
12. Wolber, J., Cherubini, A., Dzik-Jurasz, A. S., Leach, M. O. & Bifone, A. Spin-lattice relaxation of laser-polarized xenon in human blood. *Proc. Natl Acad. Sci. USA* **96,** 3664–3669 (1999).
13. Zhou, X. *et al.* Reinvestigating hyperpolarized ^{129}Xe longitudinal relaxation time in the rat brain with noise considerations. *NMR Biomed.* **21,** 217–225 (2008).
14. Spence, M. M. *et al.* Functionalized xenon as a biosensor. *Proc. Natl Acad. Sci. USA* **98,** 10654–10657 (2001).
15. Bartik, K., Luhmer, M., Dutasta, J-P., Collet, A. & Reisse, J. ^{129}Xe and ^{1}H NMR study of the reversible trapping of xenon by cryptophane-A in organic solution. *J. Am. Chem. Soc.* **120,** 784–791 (1998).
16. Huber, G. *et al.* Water soluble cryptophanes showing unprecedented affinity for xenon: candidates as NMR-based biosensors. *J. Am. Chem. Soc.* **128,** 6239–6246 (2006).
17. Stevens, T. K., Ramirez, R. M. & Pines, A. Nanoemulsion contrast agents with sub-picomolar sensitivity for xenon NMR. *J. Am. Chem. Soc.* **135,** 9576–9579 (2013).
18. Spence, M. M. *et al.* Development of a functionalized xenon biosensor. *J. Am. Chem. Soc.* **126,** 15287–15294 (2004).
19. Schroder, L., Lowery, T. J., Hilty, C., Wemmer, D. E. & Pines, A. Molecular imaging using a targeted magnetic resonance hyperpolarized biosensor. *Science* **314,** 446–449 (2006).
20. Schroder, L. *et al.* Temperature response of ^{129}Xe depolarization transfer and its application for ultrasensitive NMR detection. *Phys. Rev. Lett.* **100,** 257603 (2008).
21. Meldrum, T. *et al.* A xenon-based molecular sensor assembled on an MS2 viral capsid scaffold. *J. Am. Chem. Soc.* **132,** 5936–5937 (2010).
22. Bai, Y., Hill, P. A. & Dmochowski, I. J. Utilizing a water-soluble cryptophane with fast xenon exchange rates for picomolar sensitivity NMR measurements. *Anal. Chem.* **84,** 9935–9941 (2012).
23. Taratula, O. & Dmochowski, I. J. Functionalized ^{129}Xe contrast agents for magnetic resonance imaging. *Curr. Opin. Chem. Biol.* **14,** 97–104 (2010).
24. Taratula, O., Hill, P. A., Bai, Y., Khan, N. S. & Dmochowski, I. J. Shorter synthesis of trifunctionalized cryptophane-A derivatives. *Org. Lett.* **13,** 1414–1417 (2011).
25. Palaniappan, K. K. *et al.* Molecular imaging of cancer cells using a bacteriophage-based ^{129}Xe NMR biosensor. *Angew. Chem. Int. Ed.* **52,** 4849–4853 (2013).
26. Wei, Q. *et al.* Designing ^{129}Xe NMR biosensors for matrix metalloproteinase detection. *J. Am. Chem. Soc.* **128,** 13274–13283 (2006).
27. Kotera, N. *et al.* Design and synthesis of new cryptophanes with intermediate cavity sizes. *Org. Lett.* **13,** 2153–2155 (2011).
28. Pfeifer, F. Distribution, formation and regulation of gas vesicles. *Nature Rev. Microbiol.* **10,** 705–715 (2012).
29. Walsby, A. E. Gas vesicles. *Microbiol. Rev.* **58,** 94–144 (1994).
30. Walsby, A. E. Permeability of gas vesicles to perfluorocyclobutane. *J. Gen. Microbiol.* **128,** 1679–1684 (1982).
31. Li, N. & Cannon, M. C. Gas vesicle genes identified in *Bacillus megaterium* and functional expression in *Escherichia coli*. *J. Bacteriol.* **180,** 2450–2458 (1998).
32. Abragam, A. *Principles of Nuclear Magnetism* (Oxford Univ. Press, 1983).
33. Anet, F. A. L. & Basus, V. J. Limiting equations for exchange broadening in two-site NMR systems with very unequal populations. *J. Magn. Reson. (1969)* **32,** 339–343 (1978).
34. Soesbe, T. C., Merritt, M. E., Green, K. N., Rojas-Quijano, F. A. & Sherry, A. D. T2 exchange agents: a new class of paramagnetic MRI contrast agent that shortens water T2 by chemical exchange rather than relaxation. *Magn. Reson. Med.* **66,** 1697–1703 (2011).
35. Mazzanti, M. L. *et al.* Distribution of hyperpolarized xenon in the brain following sensory stimulation: preliminary MRI findings. *PLoS One* **6,** e21607 (2011).
36. Zhou, X. *et al.* MRI of stroke using hyperpolarized ^{129}Xe. *NMR Biomed.* **24,** 170–175 (2011).
37. Peled, S. *et al.* Determinants of tissue delivery for ^{129}Xe magnetic resonance in humans. *Magn. Reson. Med.* **36,** 340–344 (1996).
38. Martin, C. C. *et al.* The pharmacokinetics of hyperpolarized xenon: implications for cerebral MRI. *J. Magn. Reson. Imag.* **7,** 848–854 (1997).
39. Ruiz-Cabello, J., Barnett, B. P., Bottomley, P. A. & Bulte, J. W. M. Fluorine (^{19}F) MRS and MRI in biomedicine. *NMR Biomed.* **24,** 114–129 (2011).
40. Gilad, A. A. *et al.* Artificial reporter gene providing MRI contrast based on proton exchange. *Nature Biotechnol.* **25,** 217–219 (2007).
41. McMahon, M. T. *et al.* New 'multicolor' polypeptide diamagnetic chemical exchange saturation transfer (DIACEST) contrast agents for MRI. *Magn. Reson. Med.* **60,** 803–812 (2008).
42. Zabow, G., Dodd, S., Moreland, J. & Koretsky, A. Micro-engineered local field control for high-sensitivity multispectral MRI. *Nature* **453,** 1058–1063 (2008).
43. Khalil, A. S. & Collins, J. J. Synthetic biology: applications come of age. *Nature Rev. Genet.* **11,** 367–379 (2010).
44. Mandel, M. J. Models and approaches to dissect host–symbiont specificity. *Trends Microbiol.* **18,** 504–511 (2010).
45. Piwnica-Worms, D., Schuster, D. P. & Garbow, J. R. Molecular imaging of host–pathogen interactions in intact small animals. *Cell Microbiol.* **6,** 319–331 (2004).
46. Forbes, N. S. Engineering the perfect (bacterial) cancer therapy. *Nature Rev. Cancer* **10,** 785–794 (2010).
47. Schaffer, D. V., Koerber, J. T. & Lim, K. I. Molecular engineering of viral gene delivery vehicles. *Annu. Rev. Biomed. Eng.* **10,** 169–194 (2008).
48. Stuart, E. S., Morshed, F., Sremac, M. & DasSarma, S. Cassette-based presentation of SIV epitopes with recombinant gas vesicles from halophilic archaea. *J. Biotechnol.* **114,** 225–237 (2004).
49. Duhamel, G. *et al.* Xenon-129 MR imaging and spectroscopy of rat brain using arterial delivery of hyperpolarized xenon in a lipid emulsion. *Magn. Reson. Med.* **46,** 208–212 (2001).
50. Cleveland, Z. I. *et al. In vivo* MR imaging of pulmonary perfusion and gas exchange in rats via continuous extracorporeal infusion of hyperpolarized ^{129}Xe. *PLoS one* **7,** e31306 (2012).

Acknowledgements

We thank P. Dao for assistance with NMR measurements, M. Cannon for providing the pNL29 plasmid and R. Zalpuri and K. McDonald for assistance with electron microscopy. This work was supported by the Miller Research Fellowship and Burroughs Wellcome Career Award at the Scientific Interface (M.G.S.), California Institute For Regenerative Medicine grant RT2-02022 (D.V.S.) and Department of Energy contract DE-AC02-05CH11231 (A.P., V.S.B).

Author contributions

M.G.S. conceived and directed the study. M.G.S., R.M.R., V.S.B. and L.J.S. designed the experiments. M.G.S., R.M.R., J.S. and L.J.S. performed NMR measurements. M.G.S. prepared the GVs, bacteria and mammalian cells. M.G.S. and G.S. generated *E. coli* genetic constructs. M.G.S., R.M.R. and J.S. analysed the data. M.G.S. wrote the manuscript with interpretation and input from all authors. M.G.S. and V.S.B. provided supervision with input from A.P. and D.V.S.

Additional information

Supplementary information is available in the online version of the paper. Reprints and permissions information is available online at www.nature.com/reprints. Correspondence and requests for materials should be addressed to M.G.S. Correspondence may also be addressed to V.S.B.

Competing financial interests

The authors declare no competing financial interests.

© 2014 Macmillan Publishers Limited. All rights reserved.